

International Conference on Space Optics—ICSO 2018

Chania, Greece

9–12 October 2018

Edited by Zoran Sodnik, Nikos Karafolas, and Bruno Cugny



Numerical prediction and experimental validation of irradiance fluctuations in a pre-compensated optical feeder link

K. Kudielka

E. Fischer

T. Dreischer



Numerical prediction and experimental validation of irradiance fluctuations in a pre-compensated optical feeder link

K. Kudielka*, E. Fischer, T. Dreischer
Synopta GmbH, Wiesenstrasse 6, CH-9034 Eggersriet, Switzerland

ABSTRACT

This paper focuses on optical links from ground to a geostationary satellite, using adaptive optics to pre-compensate the wave-front of the uplink beam. We present the numerical prediction of the irradiance statistics at the satellite. Uplink beam diameters, as well as the turbulence strength in the boundary layer and in the tropopause are varied. Results show, that the choice of uplink beam diameter significantly affects the fading statistics, in particular the shape of the probability density function. In a realistic worst case (30° elevation, day-time turbulence, sea level), the optimum beam diameter, showing minimum irradiance fluctuation at the target, is around 20 cm. In that case, the probability of fades larger than 6 dB (with respect to the diffraction limit) is approx. 10^{-3} .

A breadboard of such a closed-loop adaptive-optics pre-compensation system has been implemented. It comprises a Shack-Hartmann wavefront sensor, two tip/tilt mirrors, a 140-element deformable mirror, a far-field propagation simulator, and two rotating turbulence phase screens (simulating tropopause and atmospheric boundary layer, respectively). The link geometry is representative of the intended application in an optical feeder link for geo-stationary satellites. Preliminary test results confirm the numerical predictions.

Keywords: Optical feeder links, adaptive optics, optical ground station

1. INTRODUCTION

The use of adaptive optics in optical ground stations for high-rate optical links from space to ground is state of the art^{1,2}. The adaptive pre-compensation of the transmitted wave-front is considered an enabling technology for high-rate optical data transmission from ground to space, and subject to extensive research – both analytically, and experimentally^{3,4,5,6,7}.

Pre-compensation technology is in development, for use in the next generation of Synopta's Adaptive Optical Ground Stations (AOGS). In order to properly size the system, we want to predict the performance of the pre-compensation, under various atmospheric conditions, for different link geometries, and for varying key system parameters (such as beam diameter). To this end, we developed a multiple-phase-screen propagation model, similar to models already published⁷. In Section 2, we present the key features of the model, the parameter set we chose for the realistic worst case in an optical ground-to-GEO uplink (driving the system design), and some validation results. In Section 3, we summarize and discuss the main results of the simulation exercise.

To gain practical experience with closed-loop adaptive-optics (AO) pre-compensation, we have implemented a suitable test bed as well, comprising two breadboards (representing AOGS, and optical space terminal, respectively), and two rotating turbulence phase plates (Section 4). We give an overview of the design, and show, that this down-scaled arrangement yields representative results in terms of uplink scintillation statistics.

2. SIMULATION MODEL

2.1 Geometry

Figure 1 shows the overall geometry of the link between a geo-stationary spacecraft and an optical ground station (OGS), along the line of sight. The simulation model consists of several planar screens, where complex optical field distributions are calculated (and potentially modified in phase) – two at each end of the link, plus several more throughout the volume covered by Earth's atmosphere (up to an altitude of 20 km). As a realistic worst case, we have chosen an elevation of 30°, and an OGS altitude around sea level.

*klaus.kudielka@synopta.ch; phone +41 44 300 10 59; www.synopta.ch

For each particular realization of the turbulent atmosphere (defined by the six turbulence phase screens shown in Figure 1), we start with a deterministic downlink beam at the top of the atmosphere – large enough to over-illuminate the OGS aperture, and small enough for accurate calculation of the Fresnel integral in the discrete domain. For the downlink, we repeatedly modify the phase of the beam, and propagate it to the next screen. Once the beam arrives at the OGS aperture, its phase distribution is conjugated, and its amplitude distribution is replaced by that of a truncated Gaussian beam, resulting in a perfectly pre-compensated uplink beam. That beam is then back-propagated through the very same phase screens (slightly shifted in lateral dimension, to simulate the point ahead angle). After passing the screen at the top of the atmosphere, the uplink beam is finally transformed into the far field, using the Fraunhofer approximation.

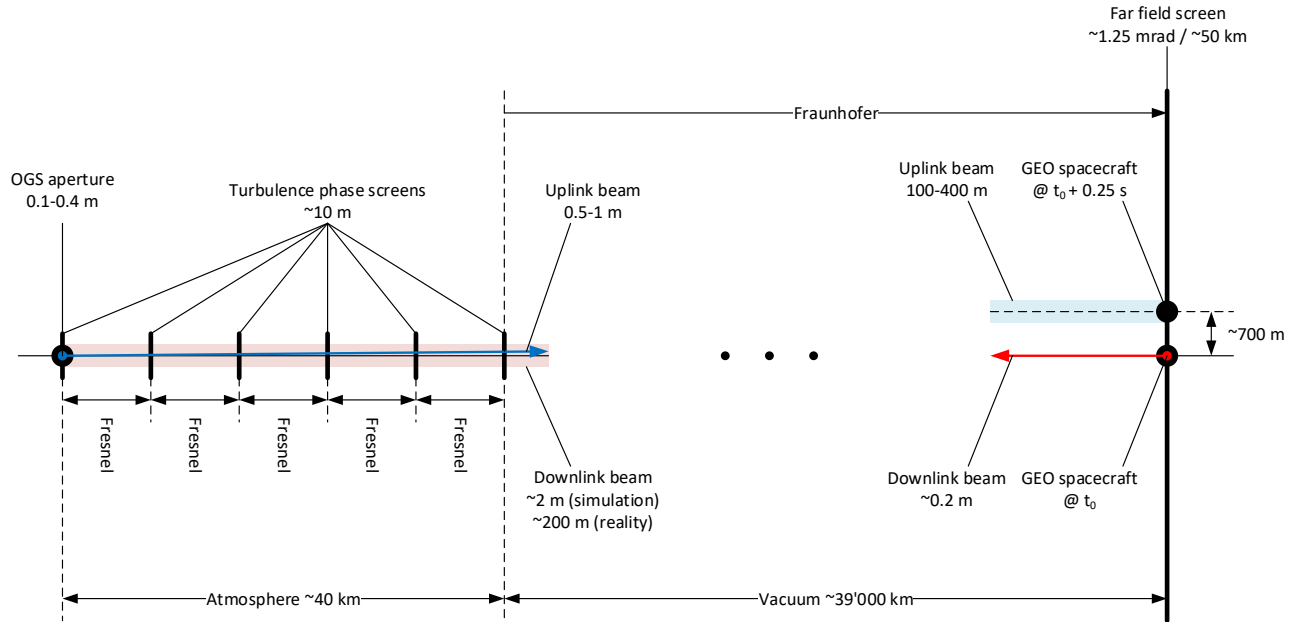


Figure 1. Simulated link geometry along the line of sight. The OGS is at sea level, the elevation of the line of sight is 30°.

2.2 Propagation between phase screens

The well-known Fresnel integral can be approximated with reasonable accuracy by the two-dimensional Discrete Fourier Transform, which is extremely well suited for efficient implementation on modern computer architectures:

$$U_{p,q} = \frac{e^{jkz}}{jN} \exp\left(\frac{j\pi}{N}(p^2 + q^2)\right) \sum_{m=0}^{N-1} \sum_{n=0}^{N-1} \left\{ U_{m,n} e^{\frac{j\pi}{N}(m^2 + n^2)} \right\} e^{-\frac{j2\pi}{N}(pm + qn)} \quad (1)$$

where

$$(\xi, \eta) = (m, n) \sqrt{\frac{\lambda z}{N}} \quad \text{and} \quad (x, y) = (p, q) \sqrt{\frac{\lambda z}{N}} \quad (2)$$

denote the physical coordinates in the source plane and the target plane, respectively. λ is the wavelength, z is the distance between neighboring phase screens, and N is the number of pixels per dimension, of the phase screen. The spatial sampling period is identical for source and target plane, and thus in general for all phase screens in the simulation. Typical parameters are $N = 8192$, $\lambda = 1550$ nm, and $z = 8000$ m, leading to a spatial resolution of approx. 1.2 mm, and a periodicity of approx. 10 m – sufficient to avoid spatial aliasing effects for the beam geometries under investigation.

2.3 Turbulence

For specifying the refractive index structure constant, as a function of altitude above sea level, h , we use a modified HV 5-7 model⁸,

$$C_n^2(h) = A \cdot \exp\left(-\frac{H_{GS}}{700 \text{ m}}\right) \cdot \exp\left(-\frac{h-H_{GS}}{H_A}\right) + B \cdot \exp\left(-\frac{h}{H_B}\right) + C \cdot h^{10} \cdot \exp\left(-\frac{h}{H_C}\right) \quad (3)$$

with the default parameters

$$H_{GS} = 0 \text{ m}, H_A = 100 \text{ m}, B = 2.7 \cdot 10^{-16} \text{ m}^{-2/3}, H_B = 1500 \text{ m}, \text{ and } H_C = 1000 \text{ m}. \quad (4)$$

For the moment, we only vary the turbulence strength in the boundary layer, A , and in the tropopause, C , which are the parameters of primary interest. Table 1 gives an overview of the atmospheric conditions used in the simulation. The resulting range of the Fried parameter, r_0 , and of the isoplanatic angle, ϑ_0 , covers the range reported from site measurements^{9,10} very well, if the measurements are extrapolated to the present link geometry.

Table 1. Atmospheric conditions used in the simulation. Fried parameter and isoplanatic angle are given for the chosen link geometry, and for a wavelength of 1550 nm.

Condition	Boundary layer	Tropopause	A	C	r_0	ϑ_0
1	Daytime	Typical	$1.7 \cdot 10^{-13} \text{ m}^{-2/3}$	$3.59 \cdot 10^{-53} \text{ m}^{-10/23}$	36.9 mm	8.62 μrad
2	Nighttime	Typical	$1.7 \cdot 10^{-14} \text{ m}^{-2/3}$	$3.59 \cdot 10^{-53} \text{ m}^{-10/23}$	127 mm	8.92 μrad
3	Daytime	Strong	$1.7 \cdot 10^{-13} \text{ m}^{-2/3}$	$1.20 \cdot 10^{-53} \text{ m}^{-10/23}$	36.6 mm	4.83 μrad
4	Daytime	Weak	$1.7 \cdot 10^{-13} \text{ m}^{-2/3}$	$10.8 \cdot 10^{-53} \text{ m}^{-10/23}$	37.0 mm	13.7 μrad

The continuous turbulence strength along the propagation path is collapsed into the six discrete phase screens, via numerical integration. Random realizations of the phase screens are calculated, using the Fourier series method¹¹, in combination with a von Karman spectrum.

2.4 Collection of statistics

In principle, the model developed is capable of generating time series of the irradiance distribution in the far field, by incrementally shifting each frozen phase screen. To this end, individual wind speed vectors could be assigned to each turbulence layer.

For this paper, we confined the analysis to accumulate statistics with high resolution, and therefore sampled the generated phase screens at a Cartesian grid of $100 \times 100 = 10000$ instances. Each simulation run therefore revealed 10000 irradiance distributions of 128×128 pixels. We evaluated probability density function (PDF), and cumulative distribution function (CDF) for the centre pixel, i.e. the nominal position of the satellite.

2.5 Model checks

In the paragraphs below, we discuss a selection of checks, which were done to gain confidence in the simulation model.

Without any turbulence, fundamental wave propagation from the OGS aperture within the bottom screen, via several intermediate Fresnel propagations, into the far field, has been verified. Gaussian, as well as uniform sources (circular aperture with or without central obscuration) have been tested, and the final far field distributions have been found to agree with the well-known analytical formulas (both in terms of shape, and of amplitude).

Turbulence phase screen generation (for a given Fried parameter, r_0) was validated with respect to analytical formulas. The residual phase error after tip-tilt removal was shown to converge at $0.134 (D/r_0)^{5/3}$ to within fractions of a percent.

Using a realistic set of 6 numerically generated turbulence phase screens, a typical downlink Gaussian beam was propagated from the top of the simulated atmosphere down to the OGS, completely conjugated in phase (without truncation or any other amplitude transformation), and back-propagated to the top of the atmosphere. As expected, the back-propagated optical field was identical with the original downlink field (to within ~ 5 digits).

Measured statistics of received power at the satellite, obtained with single-beam optical uplinks from the ESA Optical Ground Station to the ARTEMIS satellite¹², were compared with results of the simulation model (*without* pre-compensation, in order to be representative). Seeing conditions provided by independent measurements were taken as an input to the simulation. Measured and simulated PDFs agree very well.

3. SIMULATION RESULTS

For each of the four atmospheric conditions shown in Table 1, we evaluated the performance of full pre-compensation for three different uplink beam diameters, $D = \{10 \text{ cm}, 20 \text{ cm}, 40 \text{ cm}\}$, with and without point ahead, $\vartheta = \{0 \mu\text{rad},$

18 μrad }. The complete data set thus comprises $4 \times 3 \times 2 \times 10000$ far-field irradiance distributions. Throughout this paper, we present the irradiance normalized to I_{ref} , which is the diffraction limited on-axis irradiance associated with the relevant uplink beam. In other words, our reference is the case without any turbulence.

Mean value and scintillation index of the irradiance at the satellite are presented in Table 2. *Without* point ahead, the average irradiance delivered is always very close to the diffraction limit. *With* a point-ahead angle of 18 μrad , average losses are between 0.5 dB and 4 dB, depending on condition and beam diameter. With increasing beam diameter, average performance decreases in general, but the scintillation index actually improves (i.e. decreases) in most cases.

Table 2. Full pre-compensation: Mean value of the irradiance at the satellite, normalized to the diffraction limit, and the associated scintillation index. Results are shown for all atmospheric conditions, with and without point ahead, and for three different uplink beam diameters.

Condition	ϑ	$\langle I \rangle / I_{ref}$			$\sigma_I^2 = \langle I^2 \rangle / \langle I \rangle^2 - 1$		
		10 cm	20 cm	40 cm	10 cm	20 cm	40 cm
1	0 μrad	0.99	0.97	0.96	0.115	0.063	0.020
1	18 μrad	0.77	0.69	0.56	0.128	0.082	0.067
2	0 μrad	0.99	0.97	0.96	0.114	0.062	0.019
2	18 μrad	0.89	0.81	0.67	0.119	0.075	0.061
3	0 μrad	0.97	0.94	0.92	0.291	0.159	0.049
3	18 μrad	0.72	0.58	0.39	0.319	0.231	0.241
4	0 μrad	0.99	0.99	0.98	0.058	0.030	0.009
4	18 μrad	0.79	0.73	0.65	0.062	0.036	0.025

This tendency is also visualized by the associated PDFs, shown in Figure 2 for Condition 1. *Without* point ahead, larger uplink beam diameters are closer to the “ideal” case of complete phase conjugation of the (large) downlink beam, and therefore have the tendency to converge towards a normalized irradiance of 1. *With* point ahead, this effect is superimposed by a general shift towards lower irradiance levels, due to anisoplanatism. In particular, for very large uplink beams, the shape of the PDF changes from pronounced surges (typical log-normal distribution), to pronounced fades. Despite having a smaller scintillation index, we thus may experience stronger fades. In general, one should be cautious when using the scintillation index as the sole performance metric.

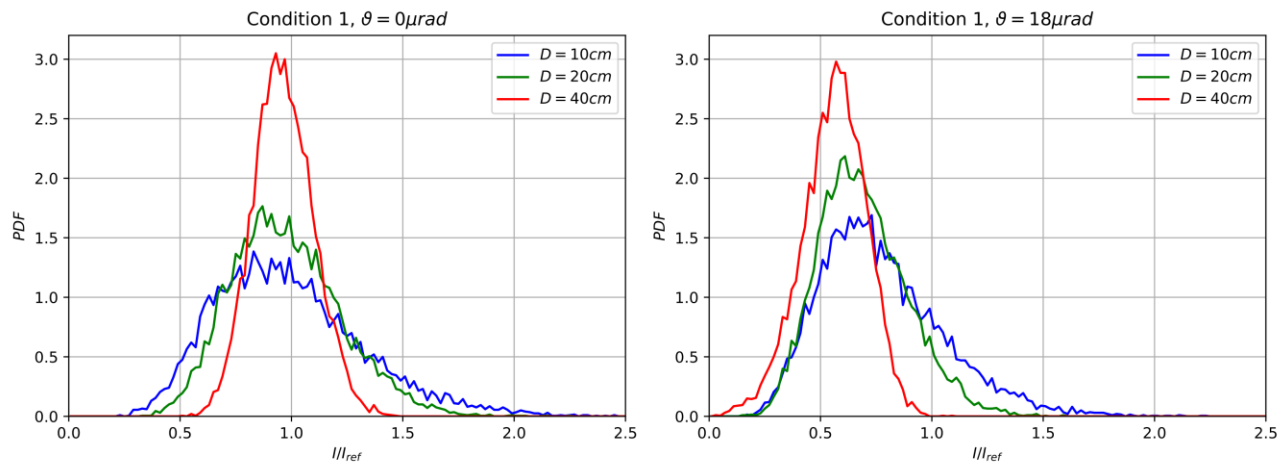


Figure 2. Full pre-compensation, atmospheric condition 1: PDF of irradiance at the satellite, normalized to the diffraction limit. Left: without point ahead; right: with point ahead.

The fundamental change from pronounced surges to pronounced fades is also evident from instantaneous irradiance distributions in the far field (Figure 3). A small uplink beam diverges significantly, while still propagating through the turbulent atmosphere. In this case, the larger beam may be re-focused by the higher layers of the atmosphere, and spots stronger than the original diffraction limit may materialize at the target. On the other hand, a large pre-compensated uplink beam diverges only marginally while propagating through the lower layers, and therefore the on-axis far field irradiance can only be degraded by anisoplanatism in the higher layers.

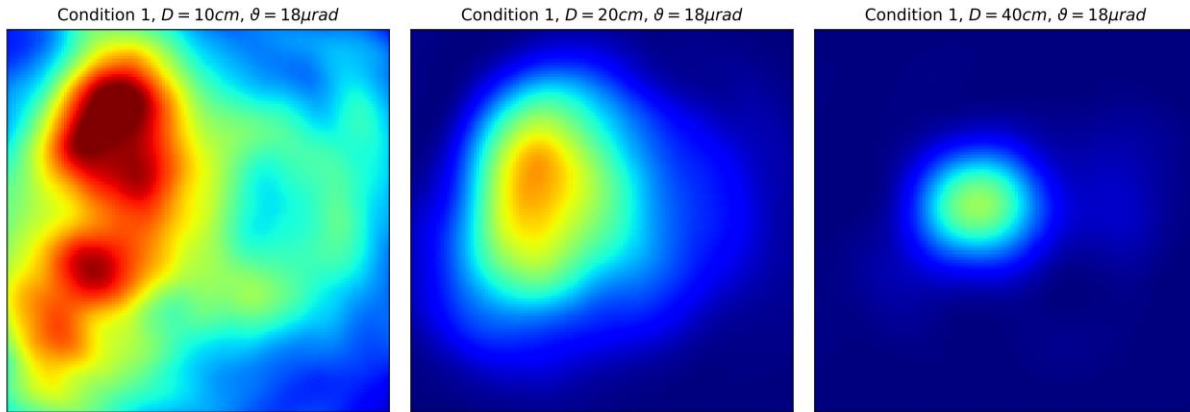


Figure 3. Full pre-compensation, atmospheric condition 1, with point ahead: Exemplary instantaneous irradiance distributions in the far field, for various uplink beam diameters, normalized to the corresponding diffraction limit. Dark blue ~ 0 , dark red \sim all levels ≥ 1 . Each image is approx. $20 \mu\text{rad} \times 20 \mu\text{rad}$. The satellite position is at the center of each image.

Figure 4 shows our main analysis result, i.e. the cumulative distribution of the normalized irradiance at the satellite, at the typical point-ahead angle for a ground-to-GEO link. The results for all four simulated atmospheric conditions are depicted, and will be discussed in the paragraphs below.

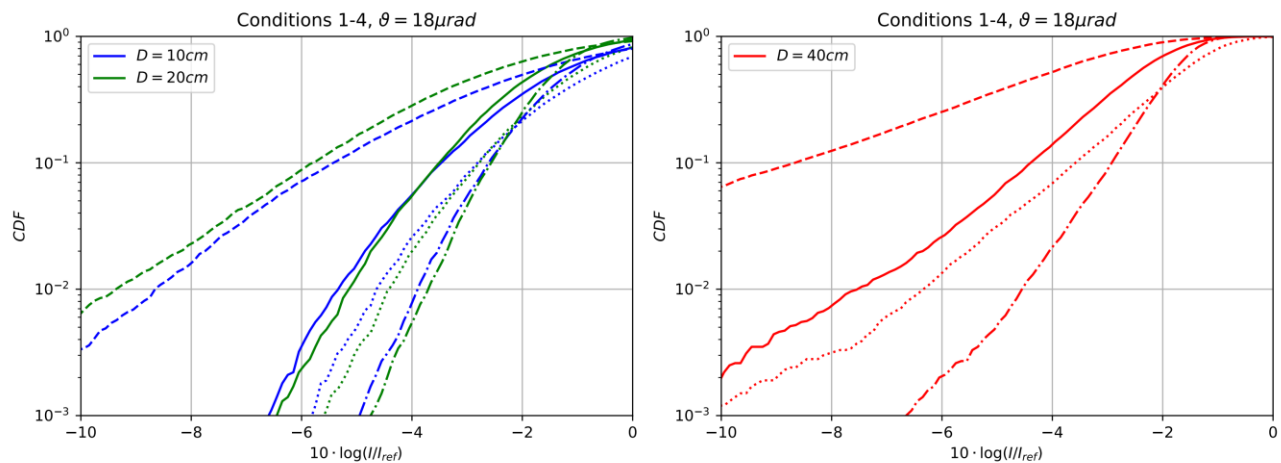


Figure 4. Full pre-compensation, with point ahead: CDF of irradiance at the satellite, normalized to the diffraction limit. Solid lines: Condition 1; dotted lines: Condition 2; dashed lines: Condition 3; dash-dotted lines: Condition 4.

Fading statistics are almost identical for $D = 10 \text{ cm}$ and $D = 20 \text{ cm}$, respectively – due to the superposition of two different an-isoplanatic effects (beam divergence and point ahead). The larger beam diameter thus provides 6 dB more antenna gain, with only marginal changes in fading probability. At $D = 40 \text{ cm}$, the probability of deep fades increases considerably, though.

Thanks to full pre-compensation of the uplink beam, the variation between Condition 1 (daytime) and Condition 2 (nighttime) is very small. A factor of 10 in turbulence strength of the boundary layer causes only 0.5 dB to 1 dB of degradation. We consider this fact very important for operational feeder links.

On the other hand, sensitivity with respect to turbulence strength in the tropopause (C parameter in the modified HV 5-7 model), is stronger for this type of uplink. A factor-3 increase (Condition 3 vs. Condition 1) may already cost about 6 dB in terms of fading threshold, at a probability of 10^{-3} . The isoplanatic angle (shown in Table 1) correlates very well with this kind of degradation, and may need supervision in an operational system with site redundancy.

As a side product of our simulation exercise, Figure 5 shows the CDF of the normalized irradiance at the satellite, if *only tip and tilt* of the uplink beam are pre-compensated. With $D = 5$ cm, we can expect similar fading statistics during daytime, as in a fully pre-compensated uplink with $D = 20$ cm (Figure 4). This 12-dB improvement in terms of antenna gain should be seriously considered for high-capacity optical feeder links to satellites in geo-stationary orbit.

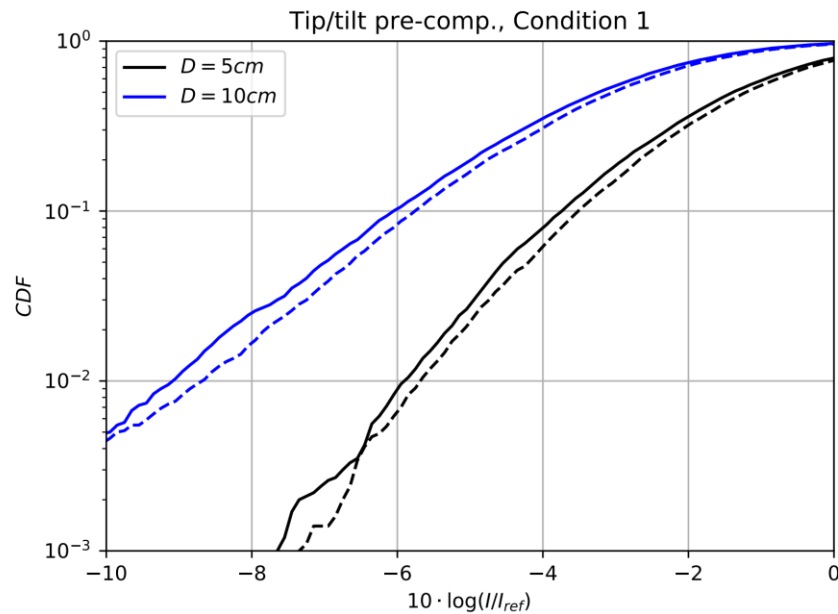


Figure 5. Tip/tilt pre-compensation, atmospheric condition 1: CDF of irradiance received at the satellite, normalized to the diffraction limit. Solid lines: $\vartheta = 18 \mu\text{rad}$; dashed lines: $\vartheta = 0 \mu\text{rad}$.

4. UPLINK PRE-COMPENSATION EXPERIMENT

Figure 6 shows a block diagram of the uplink pre-compensation experiment, implemented at Synopta premises. The setup comprises two breadboards, one representing the optical ground station, and one essentially simulating the far-field propagation between the satellite and the upper layers of the atmosphere. A single-mode fiber placed in the focal plane emits the downlink beam propagating towards the OGS, and a camera placed in the focal plane records the irradiance of the uplink beam in the simulated far field.

Numerical simulations have shown, that two properly placed discrete phase screens provide a very good approximation of the continuous turbulence along the line of sight, and result in PDFs very close to multi-screen propagation models. This fact has also been published by others⁷. One screen simulates the strong turbulence in the boundary layer, the other one simulates the turbulence in the higher layers. For practical reasons, each breadboard carries one rotating turbulence phase plate.

The Fried parameter of each phase plate was chosen, such that it covers the turbulence strength of a certain part of the atmospheric volume along the line of sight. The longitudinal position of the phase plate was chosen, such that the resulting isoplanatic angle matches the one from the continuous profile of turbulence strength in the very same part of the volume. Finally, a rigorous downscaling of the link geometry was performed, to keep all relations concerning the laws of wave propagation. Table 3 summarizes the results of the scaling exercise for atmospheric condition 1.

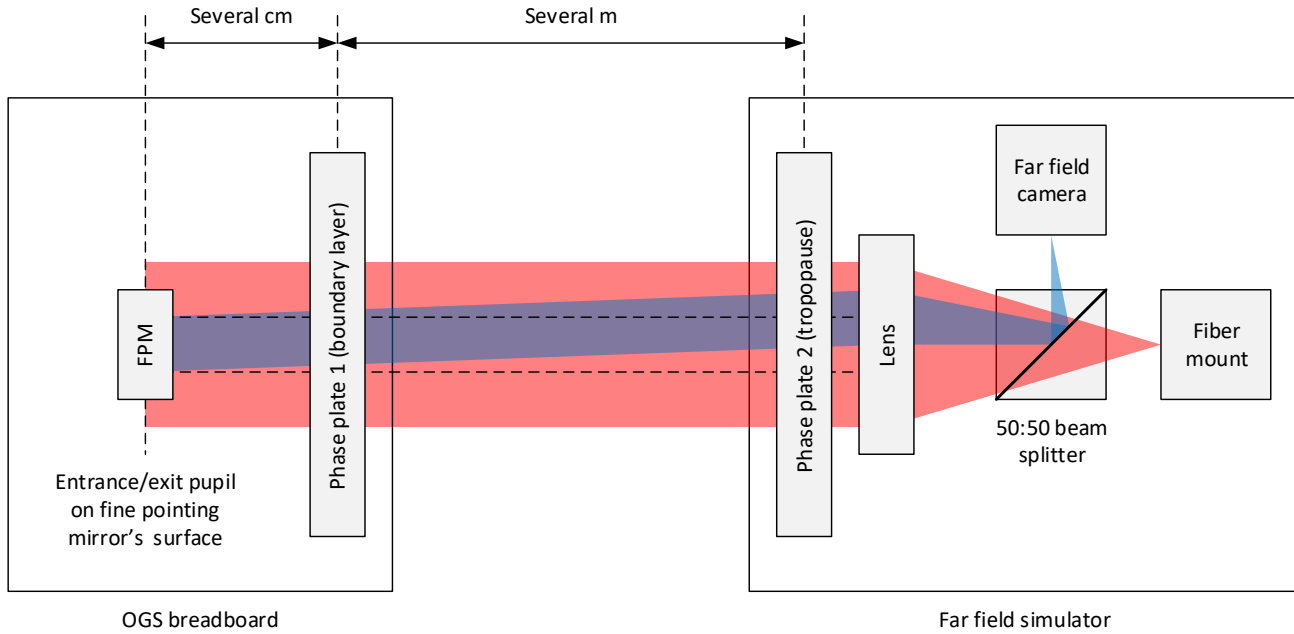


Figure 6. Setup of the uplink pre-compensation experiment, using two rotating turbulence phase plates.

Table 3. Scaling of the GEO feeder link geometry (realistic worst case) to the uplink experiment in the laboratory

Parameter	Symbol	Application	Scaling factor	Experiment
Transmit aperture diameter	D	200 mm	$a=0.022$	4.4 mm
Outer scale	L_0	10 m	a	220 mm
Fried parameter due to boundary layer ($h = 0 \dots 2$ km)	$r_{0,BL}$	37 mm	a	0.81 mm
Distance between pupil and simulated boundary layer	z_{BL}	320 m	a^2	150 mm
Isoplanatic angle due to boundary layer	$\vartheta_{0,BL}$	37 μ rad	$1/a$	1.7 mrad
Fried parameter due to upper layers ($h = 2 \dots 22$ km)	$r_{0,UL}$	490 mm	a	11 mm
Distance between pupil and simulated upper layer	z_{UL}	17 km	a^2	8.4 m
Isoplanatic angle due to upper layers	$\vartheta_{0,UL}$	9.1 μ rad	$1/a$	0.41 mrad
Point-ahead angle	ϑ	18 μ rad	$1/a$	0.82 mrad

Figure 7 shows a photograph of the OGS breadboard implemented for full pre-compensation of the uplink beam. The breadboard consists of essentially three branches. The common uplink/downlink branch comprises a fine-pointing mirror (FPM), a 140-element deformable mirror, and a polarization splitter separating uplink and downlink beams. The downlink branch comprises a field stop and a Shack-Hartmann wave-front sensor. A fibre collimator and a point-ahead mirror form the uplink branch.

Preliminary uplink tests have been conducted with the setup described here, using tip/tilt pre-compensation and one rotating phase screen (Figure 8). The results so far agree well with expectation: Fading statistics are comparable with simulation results (Figure 5), the absence of turbulence in the upper layers explains the lack of surges. As a next step, the performance of full pre-compensation will be evaluated, and compared with numerical predictions.

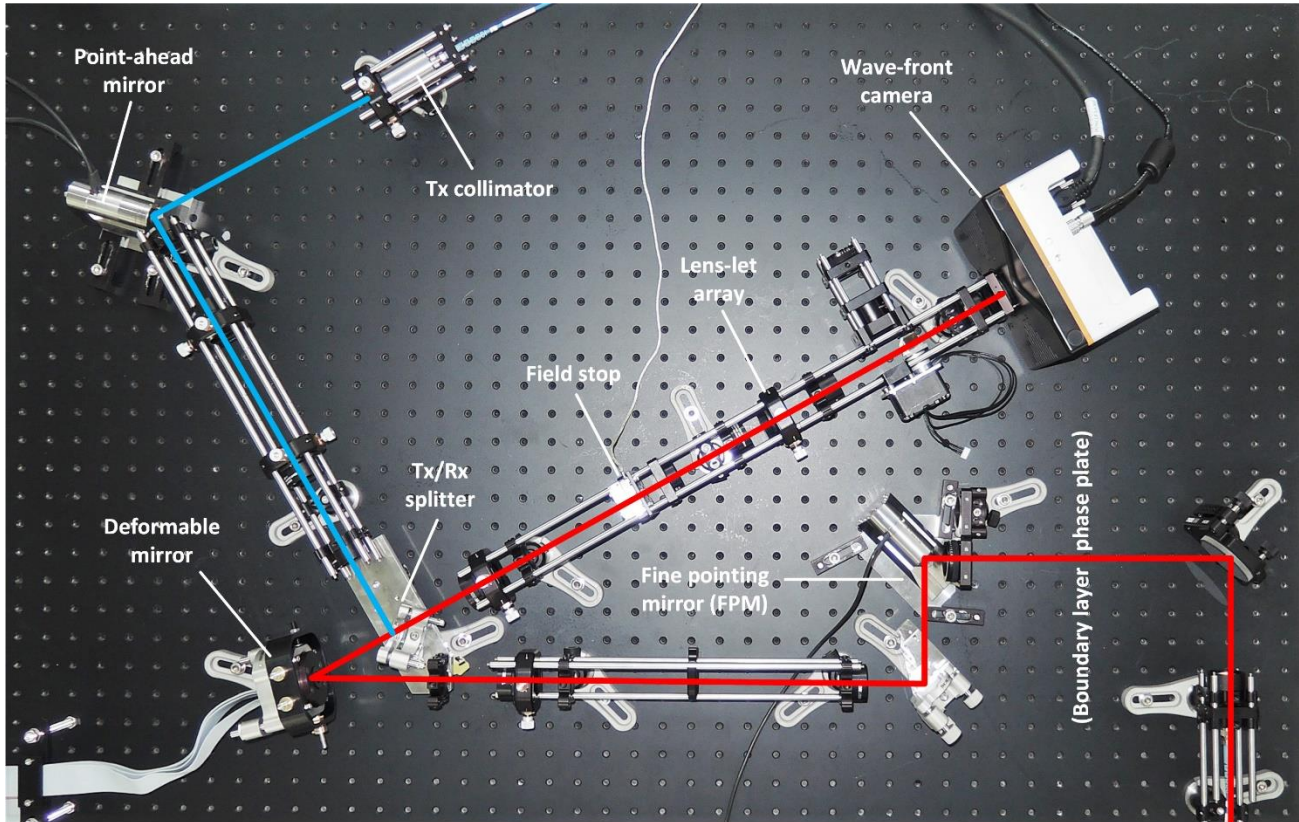


Figure 7. Annotated photograph of the OGS breadboard.

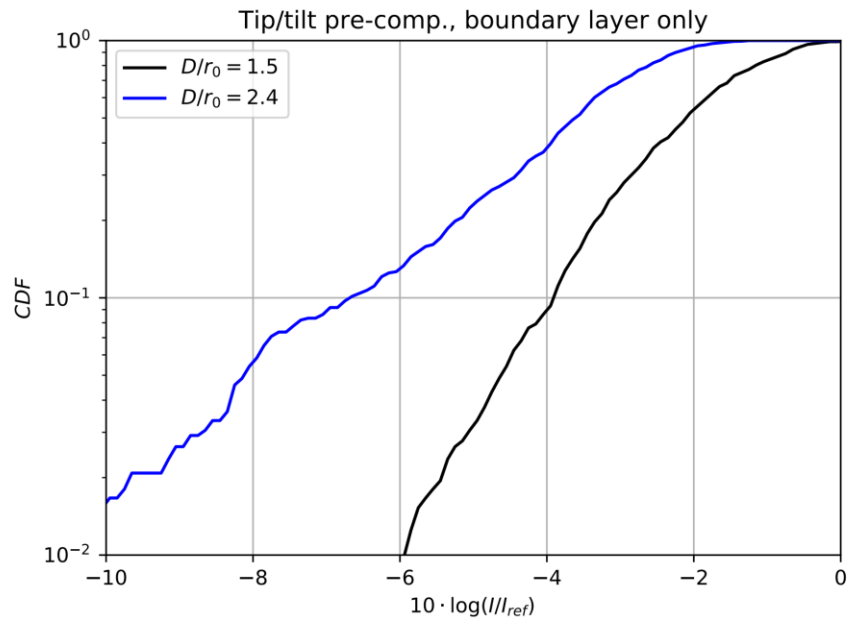


Figure 8. Test result obtained with tip/tilt pre-compensation, and the boundary-layer phase plate: CDF of irradiance received at the satellite, normalized to the diffraction limit.

5. CONCLUSIONS

We have presented the numerical prediction of the irradiance statistics at a geostationary satellite in a fully pre-compensated optical ground-to-space link, using an adaptive optical ground station. For the realistic worst case of sea-level altitude and 30° elevation, an uplink beam diameter of 20 cm seems to be a good compromise between average power transmitted, and fading statistics due to anisoplanatism. The adaptive optics has to be engineered to cope with Fried parameters as small as 37 mm, at a wavelength of 1550 nm. As long as the turbulence strength in the tropopause stays within limits (which appears to be identical with $\vartheta/\vartheta_0 \leq 2$), there is little variation of the scintillation statistics with atmospheric condition. Fades deeper than 6 dB (with respect to the diffraction limit) can be expected with a probability of 10^{-3} . Next to the Fried parameter, the isoplanatic angle is an important parameter to watch in an operational feeder link system.

6. ACKNOWLEDGEMENT

Part of this work has been carried out under ESA contract within ARTES C&G. We express our gratitude to the Swiss Space Office and to ESA for their continued support.

REFERENCES

- [1] Fischer, E., et al., "Use of Adaptive Optics in Ground Stations for High Data Rate Satellite-to-Ground Links", Proc. SPIE 10562, 105623L (2016).
- [2] Fischer, E., et al., "Upgrade of ESA Optical Ground Station with Adaptive Optics for High Data Rate Satellite-to-Ground Links", IEEE Int. Conf. on Space Optical Systems and Applications (ICSOS), 69-76 (2017).
- [3] Védrenne, N., et al., "Turbulence effects on bi-directional ground-to-satellite laser communication systems", Proc. Int. Conf. on Space Optical Systems and Applications (ICSOS), 10-1 (2012).
- [4] Leonhard, N., "Real-time adaptive optics testbed to investigate point-ahead angle in pre-compensation of Earth-to-GEO optical communication", Optics Express 24(12), 13157-13172 (2016).
- [5] Védrenne, N., et al., "Adaptive optics pre-compensation for GEO feeder links: towards an experimental demonstration", IEEE Int. Conf. on Space Optical Systems and Applications (ICSOS), 83-87 (2017).
- [6] Saathof, R., et al., "Optical Technologies for Terabit/s-throughput Feeder Link", IEEE Int. Conf. on Space Optical Systems and Applications (ICSOS), 133-139 (2017).
- [7] Camboulives, A.-R., et al., "Statistical and temporal irradiance fluctuations modeling for a ground-to-geostationary satellite optical link", Appl. Opt. 57(4), 709-721 (2018).
- [8] Giggenbach, D. "Optimierung der optischen Freiraumkommunikation durch die Atmosphäre - Focal array receiver", Ph.D. thesis, Universität der Bundeswehr, München (2004).
- [9] Walters, D. L., Bradford, L. W., "Measurements of r_0 and θ_0 : two decades and 18 sites", Appl. Opt. 36(30), 7876-7886 (1997).
- [10] Mohr, J. L., et al., "Optical Turbulence Measurements and Models for Mount John University Observatory", Publications of the Astronomical Society of Australia, 27, 347-359 (2010).
- [11] Welsh, B., "A Fourier Series Based Atmospheric Phase Screen Generator for Simulating Anisoplanatic Geometries and Temporal Evolution", Proc. SPIE 3125, 327-338 (1997).
- [12] Alonso, A., et al., "Performance of satellite-to-ground communications link between ARTEMIS and the Optical Ground Station", Proc. SPIE 5572, 372-383 (2004).